V. Investigation of edge pedestal structure in DIII-D (DoE Grant ER54538)

W. M. Stacey and R. J. Groebner

(to be published in Physics of Plasmas, 2006)

ABSTRACT

A calculation based on the requirements of particle, momentum and energy conservation, conductive heat transport and atomic physics resulting from a recycling and fueling neutral influx was employed to investigate the experimental density, temperature, rotation velocities and radial electric field profiles in the edge of three DIII-D [J. Luxon, Nucl. Fusion, 42, 614 (2002)] high-mode plasmas. The calculation indicated that the cause of the pedestal structure in the density was a momentum balance requirement for a steep negative pressure gradient to balance the forces associated with an edge peaking in the inward pinch velocity (caused by the observed edge peaking in the radial electric field and rotation velocity profiles) and, to a lesser extent, in the outward radial particle flux (caused by the ionization of recycling neutrals). Thermal and angular momentum transport coefficients were inferred from experiment and compared with theoretical predictions, indicating that thermal transport coefficients were of the magnitude predicted by neoclassical and ion-temperature-gradient theories (ions) and electron-temperature-gradient theory (electrons), but that neoclassical gyroviscous theory plus atomic physics effects combined were not sufficient to explain the inferred angular momentum transfer rate throughout the edge region.

I. INTRODUCTION

A signature feature in high performance (H-mode) plasmas is the formation of a steep gradient edge region leading to pedestals in the density and temperature profiles in the plasma edge. The edge pedestal has been a subject of strong research interest, both experimental and theoretical, over the past decade, but an understanding of the physics of the pedestal structure remains elusive today. A review of work through 2000 may be found in Ref. 1.

The motivation for understanding the edge pedestal is based, at least in part, on calculations[2,3] which indicate that because of "stiffness" in temperature profiles the performance of future tokamaks will be sensitive to the value of the density and particularly the temperature at the top of the edge pedestal. Thus, understanding the edge pedestal characteristics would seem to be a prerequisite to predicting the performance of future tokamaks.

Recent work has focused on several different aspects of understanding the physics of the edge pedestal. Investigations (e.g. Refs. 4-6) of the MHD stability of the edge pressure pedestal against ballooning and peeling (surface kink) modes have advanced the ability to predict the onset of edge-localized-mode (ELM) instabilities which momentarily destroy the edge pedestal structure. Other investigations[7-9] have employed the physical conservation, transport and atomic physics constraints to understand the mechanisms that determine the observed edge pedestal structure that exists in the absence of or in between ELMS. A particle guiding center analysis[10] was employed to explain the pedestal formation in terms of the ionization of recycling neutrals, together with orbit squeezing and the presence of an X-point transport mechanism. Other studies[11-13] investigated the possibility that the width of the steep-gradient region was associated with the neutral penetration mean-free-path. Yet other studies (e.g. Refs. 14 and 15) had the objective of developing theory-based predictive correlations of measured pedestal parameters.

This paper falls in the second category of investigations mentioned above, in which the calculation is based rigorously on the particle balance, the three components of the momentum balance, the energy balance, the neutral transport equations that calculate the atomic physics terms in these equations, and the conductive heat transport relation $q = -n\chi\nabla T$; i.e. on "physical conservation, transport and atomic physics constraints". We extend our previous calculation of density and temperature profiles[7-9] to include the calculation of rotation velocities and the radial electric field in the plasma edge.

Such a calculation model is correct to the extent that all particle, torque, and energy sources are included, that all the cross-field energy and momentum transport processes are included, and that the approximations made in implementation are adequate. Therefore, it can be employed, together with experimental data, to relate the various measured profiles in the plasma edge for the purpose of identifying any missing particle, torque or energy sources and thermal and momentum transport processes

in the model, and to identify the cause-and-effect relations that determine the edge pedestal structure, which are the overarching objectives of this paper. We employ this calculation model: i) to infer thermal and momentum transport coefficients from experiment for comparison with theoretical predictions; ii) to check the agreement of the measured density, temperature, rotation velocities and radial electric field profiles with profiles calculated from these physical conservation, transport and atomic physics constraints, for the purpose of identifying any missing phenomena in the model; and iii) to interpret the causes of various features in the profiles (e.g. the density pedestal structure).

II. EDGE DENSITY & TEMPERATURE PROFILES

A. DIII-D shot parameters

We have chosen for detailed analysis a pair of heavily gas-fueled "density limit" shots (#97979 and #98893), with steep density pedestals and low to modest pedestal temperatures, and a quite different shot (#118583) with modest pedestal density and high pedestal temperatures. This choice of shots was guided by the wish to include shots with different neutral particle influxes1[11-13] and plasma shapes[16,17] . The parameters of these shots are given in Table 1.

These shots have quite different collisionality profiles in the plasma edge, as shown by the normalized ion-impurity collision frequency in Fig. 1, which might be expected to cause somewhat different profiles in other variables. Here and in subsequent figures the separatrix is at 1.0.

Table 1 Parameters of DIII-D Shots (R=1.71-1.77 m, a=0.6 m)

Shot	q_{95}	κ	δ	P_{nb} (MW)	f_{carb} (%)	n_{ped} (m^{-3})	T_{eped} (eV)	B (T)	I (MA)
97979	3.9	1.7	0.75	6.5	1.1	6.3	525	1.6	1.4
98893	4.2	1.8	0.14	2.1	0.8	8.3	120	1.6	1.2
118583	3.8	1.8	0.37	9.2	6.0	2.8	720	1.9	1.4

B. Requirement on pressure gradient

We found previously[7-9] that momentum balance and particle conservation requirements led to a constraint on the radial pressure gradient which for a two-species ion-impurity (i-I) model is of a simple pinch-diffusion form for the main ion species

$$L_{pi}^{-1} \equiv -\frac{1}{p_i^0}\frac{dp_i^0}{dr} = \frac{V_{ri} - V_{pinch,i}}{D_i} \tag{1}$$

where $V_{ri} = \Gamma_{ri}/n_i^0$ is the radial particle velocity and $V_{pinch,i}$ is a collection of terms

$$V_{pinch,i} = \frac{\left[-M_{\phi i} - n_i e_i E_\phi^A + n_i m_i \left(\nu_{iI} + \nu_{di}^*\right)\left(f_p^{-1} V_{\theta i} + E_r/B_\theta\right) - n_i m_i \nu_{iI} V_{\phi I}\right]}{n_i e_i B_\theta} \tag{2}$$

which arises in the derivation from momentum balance, $M_{\phi i}$ is the external momentum input (e.g. from neutral beams), E_ϕ^A is the induced toroidal electric field, ν_{iI} is the interspecies collision frequency, ν_{di}^* is the total frequency for radial momentum transfer by viscous, inertial, atomic physics and 'anomalous' processes, $f_p \equiv B_\theta/B_\phi$, and the other notation is standard. The quantity

$$D_i = \frac{m_i T_i \nu_{iI}}{\left(e_i B_\theta\right)^2}\left[1 + \frac{\nu_{di}}{\nu_{iI}} - \frac{Z_i}{Z_I}\right] \tag{3}$$

is of the form of a diffusion coefficient. While the nomenclature 'pinch velocity' and 'diffusion coefficient' is used because Eq. (1) has the form of a pinch-diffusion relation for the particle flux

$\left(n_i V_{ri} = -\left(D_i/T_i\right)\left(dp_i/dr\right) + n_i V_{pinch,i}\right)$, we stress that Eqs. (1)-(3) were derived from momentum and particle balance requirements[7].

The relatively simple form of Eq. (1) resulted because of the assumption that the impurity ion density distribution was the same as for the main ions and that the temperatures were the same. If these assumptions are relaxed, a more general matrix pinch-diffusion relation is obtained[7].

C. Requirements on temperature gradients

The heat conduction relations may be written as transport requirements on the temperature gradient scale lengths

$$L_{Ti,e}^{-1} = \frac{1}{\chi_{i,e}}\left[\frac{Q_{i,e}}{n_{i,e}T_{i,e}} - \frac{5}{2}\frac{\Gamma_{i,e}}{n_{i,e}}\right] \tag{4}$$

where Q_j is the total heat flux for species "j", and then subtraction of Eq. (4) from Eq. (1) yields a requirement on the density gradient scale length $L_{ni}^{-1} = L_{pi}^{-1} - L_{Ti}^{-1}$.

D. Particle and heat flux, density and temperature profile calculations

The heat and particle balance equations may be integrated inwards from the separatrix, using experimental separatrix boundary conditions, to obtain the $Q_{i,e}\left(r\right)$ and $\Gamma\left(r\right)$ profiles[7-9] that are needed to evaluate Eqs. (4) and V_{ri}. This procedure takes into account the effect of atomic physics and radiation cooling in reducing the non-radiative heat fluxes with increasing radius and the effect of the ionization of recycling (and beam deposited) neutrals in increasing the particle flux with radius.

The gradient scale lengths can then be evaluated as a function of position from the above relations, and the definitions $-\left(1/n\right)\left(dn/dr\right) = L_n^{-1}$ and $-\left(1/T_{i,e}\right)\left(dT_{i,e}/dr\right) = L_{Ti,e}^{-1}$ can be integrated inward from the separatrix, using experimental separatrix boundary conditions, to obtain the $n\left(r\right)$ and $T_{i,e}\left(r\right)$ profiles[7-9].

Since these equations and the equations for the neutral density profile are coupled, the calculation is performed iteratively.

These equations are solved on a circular cross section toroidal model in which the model minor radius r is related to the non-circular plasma minor radius r' in the horizontal mid-plane by the mapping $r = r'\sqrt{1/2\left(1+\kappa^2\right)}$ that defines an effective circle that preserves the surface area of an ellipse of elongation κ with horizontal midplane radius r'. The normalized radius $\rho = r/a$ (where a is related to plasma horizontal radius a' by the same mapping) is then identified with the flux surface function ρ for the purpose of comparison with experiment.

E. Neutral transport

In order to evaluate the atomic physics particle sources and cooling terms in the particle and energy balance equations and to evaluate the charge-exchange/recombination enhancement of the radiation function for the carbon impurities, it is necessary to calculate the neutral deuterium concentration in the edge plasma. We employ a global code[18] which i) performs core plasma particle and power balance calculations (including beam heating and particle sources, neutral influx and radiative cooling) to determine the outward plasma particle and heat fluxes across the separatrix into the SOL, which ii) are input to a "2-point" divertor model (including atomic physics and radiative cooling, particle sources and momentum sinks) to calculate the background plasma density and temperature in the SOL and divertor and the ion flux incident on the divertor target plate, which in turn iii) determines the recycling neutral particle source for a 2D neutral transport calculation[19] that provides the neutral influx and density in the plasma edge. The neutral transport model explicitly represents the poloidal asymmetry of the neutral influx arising from the divertor plate recycling source and from external fueling sources. A

more detailed discussion of the neutral transport model and comparison with DIII-D neutrals measurements and Monte Carlo calculations can be found in Ref. 19.

F. Experimental input to calculations

In order to solve the six non-linear 1D differential equations and the 2D neutral transport equations described above for the radial profiles of the plasma quantities $n, T_{i,e}, Q_{i,e,} \Gamma$ and the neutral density n_o in the edge region inside the separatrix, it is necessary to know the heat and momentum transport coefficients $\left(\chi_{i,e}, \nu^*_{di,I}\right)$ and the rotation velocities and radial electric field profiles in the plasma edge, which latter enter Eq. (2) for the 'pinch velocity'. Note that the particle transport (diffusion) coefficient of Eq. (3) is determined as part of the calculation.

Since one of our purposes in this section is to determine if the measured density and temperature profiles can be calculated from the physical conservation, transport and atomic physics constraints, and the experimental rotation velocities and radial electric field profiles, we use experimental values of the rotation velocities and radial electric field profiles $\left(E_r = E_r^{ex}, V_{\theta i} = V_{\theta I} = V^{ex}_{\theta carb,} V_{\phi i} = V_{\phi I} = V_{\phi carb}\right)$, as well as experimental values of $n\left(r_{sep}\right), T_{i,e}\left(r_{sep}\right)$ and power and particle balance values of $Q_{i,e}\left(r_{sep}\right), \Gamma\left(r_{sep}\right)$ at the separatrix, in the calculations of the $n, T_{i,e}, Q_{i,e,} \Gamma$ profiles discussed in this section.

G. Inference of heat transport coefficients from experiment

In order to calculate density, temperature and rotation profiles from the above equations we need to know the values of the heat, χ_j, and momentum, ν^*_{dj}, transport coefficients. The heat transport coefficient profiles for the main ions and electrons can be inferred from measured temperature gradients, densities and temperature, and calculated particle and heat fluxes. Conceptually, Eq. (3) can be rewritten as

$$\chi_{i,e} = L_{Ti,e}\left[\frac{Q_{i,e}}{n_{i,e}T_{i,e}} - \frac{5}{2}\frac{\Gamma_{i,e}}{n_{i,e}}\right] \tag{5}$$

and the experimental gradients can be used to infer the heat conductivities, if the density, temperatures, and heat and particle fluxes are known. In practice, we have varied the $\chi_{i,e}$ and repeated the entire solution procedure described in the previous sections until the calculated temperature profiles were in reasonable agreement with experiment; i.e. we have treated the $\chi_{i,e}$ as adjustable parameters chosen to predict the experimental temperature profiles, within the context of the overall calculation. As such, these inferred values of the transport coefficients have intrinsic interest in their own right for comparison with theoretical predictions.

We previously found[7,9] that inferred heat transport coefficients (using a less sophisticated procedure of inference) did not vary greatly over the edge region for the DIII-D shots that we have examined, so we used a single value of $\chi_{i,e}$ over the entire steep-density-gradient region and another single value over the flattop density region (in fact, we found the same value can be used over both regions in two of the three shots). This procedure could, of course, be fine-tuned by adjusting transport coefficients pointwise to obtain a more exact match to the measured temperature profiles, but this is not necessary for the purposes of this paper.

The heat transport coefficients thus inferred from experiment are given in Figs. 2. For shots 97979 and 118583, constant values of χ_i and χ_e over the entire edge region $\rho > 0.85$ (including both the steep-density-gradient and flattop density regions) sufficed for the calculated temperature profiles to match the measured values, while somewhat different constant values in the sharp-gradient and flattop density regions were needed to get a good match for shot 98893. The resulting calculated ion and electron temperature distributions are compared with measured values in Figs. 3 and 4.

The inferred constant value of the heat transport coefficients shown in Figs. 2a and 2c differ from the usual inference (e.g. Ref 20) that the steep gradient observed in the edge temperature pedestal (more pronounced for the electrons than the ions) is due to a sharply decreasing with radius value of $\chi_{i,e}$. Figures 3a and 3c, and to a lesser degree Figs. 4a and 4c, show that a single value of $\chi_{i,e}$ suffices to produce a reasonable match to the measured temperature profiles in shots 97979 and 118583 in both the "flattop" and "steep-gradient" regions. While the temperature pedestals are not as sharp as the density pedestals in these shots, these results clearly show that a sharp reduction in the transport coefficient in the steep-gradient region just inside the separatrix is not a necessary condition for an edge temperature pedestal. We defer a discussion of the cause of the temperature pedestal in these shots until a later section.

We note that the magnitudes of the inferred $\chi_{i,e}$'s in both the "flattop" and "steep-gradient" edge regions are significantly smaller than are usually inferred in both the core plasma of H-mode discharges and in the edge plasma of L-mode discharrges consistent with the usual observation of reduced thermal diffusivity in the edge regions of H-mode discharges.

For comparison with theory, Chang-Hinton neoclassical (w/orbit squeezing) and ITG mode predictions of the deuterium ion heat transport coefficients and the ETG mode prediction of the electron heat transport coefficients are also shown in Figs. 2 . These heat transport coefficient predictions, expressions for which are given in appendix A, are certainly 'in the ballpark', and the agreement of the ETG χ_e with the value inferred from experiment for the low collisionality shot 118583 is remarkable. These comparisons encourage the suggestion that more detailed transport calculations be undertaken to understand the transport in the edge plasma.

H. Inference of momentum transfer rates from experiment

In order to evaluate Eqs. (1)-(3) for the pressure gradient, we need to know the momentum transfer frequency ν^*_{dj}. This quantity can be inferred from the measured toroidal rotation velocity.

The flux surface average of the toroidal component of the momentum balance equation for each ion species 'j' can be written

$$n_j^0 m_j \nu_{jk}^0 \left(\left(1+\beta_j\right) V_{\phi j}^0 - V_{\phi k}^0 \right) = n_j^0 e_j E_\phi^A + e_j B_\theta^0 \Gamma_j + M_{\phi j}^0 \equiv n_j^0 m_j \nu_{jk}^0 y_j \,, \qquad (6)$$

where $M_{\phi j}$ is the momentum input from the neutral beams, $M_{\phi j}^{nb}$, and possibly from other "anomalous" mechanisms, $M_{\phi j}^{anom}$, and the radial transfer of toroidal momentum by viscous, inertial, and atomic physics and perhaps other processes is represented by the parameter

$$\beta_j \equiv \frac{\nu_{dj}^0 + \nu_{nj}^0 + \nu_{ionj,nb}^0 + \nu_{ionj}^0 + \nu_{elcx,j}^0 + \nu_{anom,j}}{\nu_{jk}^0} \equiv \frac{\nu_{dj}^0 + \nu_{nj}^0 + \nu_{atom,j}^0 + \nu_{anom,j}}{\nu_{jk}^0} \equiv \frac{\nu_{dj}^*}{\nu_{jk}^0} \qquad (7)$$

where

$$\nu_{dj}^0 \equiv \left\langle R^2 \nabla\phi \cdot \nabla \cdot \boldsymbol{\pi}_j \right\rangle \Big/ R_0 n_j^0 m_j V_{\phi j}^0 \qquad (8)$$

is the frequency for the radial viscous transport of toroidal angular momentum,

$$\nu_{nj}^0 \equiv \left\langle R\nabla\phi \bullet \left(n_j m_j \left(\mathbf{V}_j \bullet \nabla \right) \mathbf{V}_j \right) \right\rangle \Big/ R_0 n_j^0 m_j V_{\phi j}^0 \qquad (9)$$

is the frequency for the radial transport of toroidal angular momentum due to inertial effects, $\nu_{atom,j}^0$ is the frequency for loss of toroidal momentum due to atomic physics processes (ionization, charge-exchange, elastic scattering), and $\nu_{anom,j}$ is the frequency for loss of toroidal momentum by "anomalous" processes (e.g. turbulent transport, ripple viscosity).

The ion-electron friction term has been neglected, a sum over other species 'k' is implied in general, and the collisional momentum conservation requirement $n_j^0 m_j \nu_{jk}^0 = n_k^0 m_k \nu_{kj}^0$ has been used in writing Eq. (6). The "0" superscript denotes the flux surface averaged value.

In the above formulation, we have distinguished between external angular momentum torque sources or sinks $\left(RM_{\phi j}, Rn_j e_j E_\phi^A, \mathrm{Re}_j B_\theta \Gamma_{rj} \right)$ which do not depend on the rotation velocity, on one hand, and angular momentum loss rates due to neoclassical viscosity, inertia and atomic physics processes of the form $Rn_j m_j \nu_d V_{\phi j}$ which do depend on the rotation velocity. The latter processes are "drag" processes which can reduce, but not reverse, the predominant direction of toroidal rotation velocity determined by the direction of the neutral beam injection, while the torque input processes are capable of increasing, decreasing or reversing the toroidal velocity.

Our objective in this section is to use the measured toroidal rotation velocity (for C VI) in Eq. (6) to infer a value of the quantity ν_{dj}^*, then calculate the neoclassical gyroviscous, inertial and atomic physics ν_{dj} for comparison, and attribute any difference to "anomalous" transport processes. We note that the observation of toroidal rotation in plasmas without neutral beam injection or other obvious sources of torque input implies that there are "anomalous" input torques present under certain conditions. (Here we are using "anomalous" in the usual sense of "not understood", rather than not understandable.) We could, alternatively, solve Eq. (6) for $M_{\phi j}^{anom}$ by using a calculated ν_{dj}^*, but this would have the problem of neglecting the possibility of any other momentum transport processes increasing ν_{dj}^*. Since there is no way to solve one equation for two unknowns, we elect to infer ν_{dj}^* from Eq. (6), with the caveat that we may thereby be forcing an "anomalous" torque input process to be represented by an "anomalous" angular momentum loss rate formalism.

The toroidal momentum balance equations, Eqs. (6), can be solved for the main and impurity ion momentum transfer, or "drag", frequencies

$$\nu_{di}^* = \frac{\dfrac{M_{\phi i}^0}{n_i^0 m_i} + \dfrac{e_i}{m_i} E_\phi^A + \dfrac{e_i}{m_i} B_\theta^0 V_{ri} - \nu_{iI}^0 \left(V_{\phi i}^0 - V_{\phi I}^0 \right)}{V_{\phi I}^0 - \left(V_{\phi i}^0 - V_{\phi I}^0 \right)} \tag{10}$$

and

$$\nu_{dI}^* = \frac{\dfrac{M_{\phi I}^0}{n_I^0 m_I} + \dfrac{e_I}{m_I} E_\phi^A + \nu_{iI}^0 \left(V_{\phi i}^0 - V_{\phi I}^0 \right)}{V_{\phi I}^0} \tag{11}$$

in a 2-species model, where $V_{rI}^0 = 0$ has been assumed. Alternatively, a single drag frequency applicable to both ion species can be evaluated by adding the two Eqs. (6) for ions and impurities to obtain

$$\nu_d^* = \frac{\left(M_{\phi i} + M_{\phi I} \right) + e\left(n_i Z_i + n_I Z_I \right) E_\phi^A + n_i e Z_i B_\theta V_{ri}}{\left(n_i m_i + n_I m_I \right) V_{\phi I} + n_i m_i \left(V_{\phi i} - V_{\phi I} \right)} \tag{12}$$

The measured carbon rotation velocity can be used to evaluate $V_{\phi I}^0 = V_{\phi carbon}^{\exp}$ in the above equations. However, we do not know the ion toroidal velocity from experiment. We could subtract the radial components of the momentum balance equations for each ion species

$$\left(E_r^0 \Big/ B_\theta^0 \right) = V_{\phi j}^0 - f_p^{-1} V_{\theta j}^0 + P_j^{0'} \tag{13}$$

where

$$P_j^{0'} \equiv \frac{1}{B_\theta^0 n_j^0 e_j} \frac{\partial p_j^0}{\partial r}, \tag{14}$$

to evaluate the velocity difference

$$\left(V_{\phi i}^0 - V_{\phi I}^0\right) = \left(V_{\theta i}^0 - V_{\theta I}^0\right) f_p^{-1} - \left(P_i^{0'} - P_I^{0'}\right) \tag{15}$$

However, this requires knowledge the poloidal velocities, one of which (C VI) is measured, but with considerable uncertainty, and the other of which is not measured. Thus, for the purpose of evaluating the inferred momentum transport frequency, the toroidal velocity difference term in Eq. (12) is set to zero.

We note that the difference in toroidal rotation velocities for deuterium and carbon has been calculated from Eq. (15) to be significant in some low collisionality DIII-D shots[21]. When we calculated separate toroidal rotation velocities for deuterium and carbon ions for the shots considered in this paper, they were identical for the higher collisionality shots #97979 and #98893, but differed somewhat for the less collisional shot #118583, as discussed in a later section. We further note that the error introduced by this approximation is of the order of the difference in species rotation velocities, not of the order of the rotation velocities, and is small for these shots.

The experimental angular momentum radial transfer frequency of Eq. (12) is plotted for the edge region of shots #97979 and #98893 in Figs. 5. Also shown for comparison are the calculated atomic physics angular momentum loss frequency, $\nu_{atom,j}^0 = \nu_{ionj,nb}^0 + \nu_{ionj}^0 + \nu_{elcx,j}^0$, neoclassical gyroviscous angular momentum transport frequency, $\nu_{gyro,j}$, and inertial transfer frequency, ν_{nj}^0, the latter two being defined in appendix B. It would appear that atomic and neoclassical momentum transfer processes are not large enough to account for the experimentally inferred momentum transfer rate throughout the steep-gradient and flattop regions of the plasma edge in these discharges, although they become large enough to do so just inside the separatrix. We further note that the form of the gyroviscosity used in this paper, which depends only on flow gradients, may over-predict momentum transport in regions of subsonic flow with steep gradients[22] such as these edge regions. We interpret these results as evidence that some additional "anomalous" moment transport (e.g. magnetic braking, ripple viscosity, turbulent transport) or torque input processes must be involved, at least further inside the separatrix.

For shot #118583, the carbon toroidal rotation velocity reversed direction and became negative over $0.92 \le \rho \le 0.97$, possibly indicating the presence of an "anomalous" input torque. On the other hand, Eq. (15) allows the possibility that the deuterium ions, which constitute the majority of the plasma mass, were rotating in the direction of beam injection but the pressure gradient and poloidal velocity differences reversed the rotation of the impurity ions. For consistency with the treatment of the other two shots, the drag frequency was determined from Eq. (12) with the same $V_{\phi i}^0 = V_{\phi I}^0 = V_{\phi carbon}^{\exp}$ assumption, which correctly incorporated the effect of the experimental toroidal rotation velocity into the overall calculation, but resulted in a negative value of the inferred ν_{dj}^* over this radial interval of negative rotation velocity.

I. Cause of the pedestal structure

With reference to Eq. (2), the pinch velocity depends on 1) the momentum input due to the beams and to the toroidal electric field, 2) the toroidal rotation velocity for the impurity species, 3) the radial electric field, and 4) the poloidal rotation velocity of the deuterium ions. (We note that this expression may be written in different ways by making use of the above radial and toroidal momentum equations; this particular form has been chosen to best make use in its evaluation of measured quantities.) The beam momentum input was calculated from a simple beam attenuation model, and the induced toroidal electric field was measured; both contributions were small. The carbon toroidal rotation velocity and the radial electric field were determined from experiment. Consistent with the assumption $V_{\theta i} = V_{\theta I} = V_{\theta carb}^{ex}$ made

in this section, the deuterium poloidal velocity that enters the equation was evaluated from the measured carbon poloidal velocity, introducing an error of order of the difference $V_{\theta i} - V_{\theta carb}^{ex}$. The contributions of these different terms to the pinch velocity are plotted in Figs. 6a and 6b for shots #97979 and #98893. In both shots there is a strong negative peaking in the pinch velocity just inside the separatrix that is driven mainly by the radial electric field, but also in part by edge peaking in the rotation velocities.

As shown in Eq. (1), the pressure gradient is determined by the difference in the forces associated with the (outward) radial particle flux and the (inward) pinch velocity. The radial deuterium ion velocity $V_{ri} = \Gamma / n_i$ peaks just inside the separatrix because of the peaking in Γ due to the ionization of recycling and fueling neutrals and because of the decrease in n_i. As discussed above, the pinch velocity has a strong negative peaking just inside the separatrix. These two effects add to produce a strong negative pressure gradient just inside the separatrix that decreases with distance from the separatrix, as shown in Figs.6c and 6d. We note that $V_{ri} = \Gamma / n_i$ is the ion velocity that would be measured if it were possible to do so, but that V_{pinch} is a constructed quantity and that no particles would actually be found moving with this velocity; diffusion down the density gradient is driving particles outward and V_{pinch} is driving them inward—the resultant is V_r.

Since the ion pressure gradient is much steeper than the ion temperature gradient $L_{pi}^{-1} \gg L_{Ti}^{-1}$ just inside the separatrix, but the two become comparable further inside the separatrix, the ion density gradient $L_{ni}^{-1} = L_{pi}^{-1} - L_{Ti}^{-1}$ is large just inside the separatrix but becomes small with increasing distance inside the separatrix. When $-(1/n_i)(dn_i/dr) = L_{ni}^{-1}$ is then integrated inward from the separatrix, using an experimentally determined separatrix boundary condition, the resulting electron density profiles shown in Figs. 7 are obtained. These clearly are in sufficiently good agreement with the measured (Thomson) density profiles to support the conclusion that the edge pedestal density structure is a consequence of the requirement of Eq. (1) on the edge pressure gradient, given the experimentally determined rotation velocities and radial electric field profiles. It does not, of course, explain the cause of the experimentally inferred transport coefficients nor of the measured rotation velocities and radial electric fields that were used as input for the calculations. We will return to this latter matter in the next section.

The usual explanation for the cause of temperature pedestals is based on the heat fluxes in the edge "flattop" and "steep-gradient" regions being approximately the same and both satisfying the conductive relation $q = -n\chi\, dT/dr = const$. Since dT/dr is much larger in the pedestal "steep-gradient" region than in the "flattop" region, the product $n\chi$ must be proportionally smaller in the "steep-gradient" than in the "flattop" region. The conventional wisdom is that this requires that χ be smaller in the "steep-gradient" than "flattop" region. However, in these shots n is observed and calculated to decrease rapidly with radius just inside the separatrix, and a constant value of χ over the flattop and steep gradient regions was inferred from experiment for two of the shots, as discussed previously. Thus, we conclude that the main cause of the steep gradient that causes the temperature pedestal (at least for T_e) in these shots is the requirement that the temperature gradient must increase to offset the decrease of density in the steep gradient region. In other words, the temperature pedestals are required by heat removal requirements to exist because there is a density pedestal.

We have discussed the calculations of this section in sequence, as if one followed the other, for the sake of exposition. It is necessary to emphasize that this was not the case. The equations are coupled and non-linear, and they had to be solved by iterating to convergence.

J. Role of neutrals in pedestal formation

The calculated edge neutral density profiles are shown for the three shots in Fig. 8. Comparison of Figs. 7 and 8 clearly indicate that the shot (#98893) with the largest pedestal density and most rapidly attenuated neutral density profile inside the separatrix is also the shot with the steepest edge density gradient and smallest edge density width, and conversely that shot #118583 with the smallest pedestal density and weakest neutral density attenuation has the largest pedestal width. Also the effective neutral attenuation mean free path (the distance over which the neutral density attenuates by a factor of e^{-1}) in all three shots is comparable to the pedestal width, as has been noted previously[11-13]. However, by

comparison with Figs. 6, we also note that the phenomena which cause the steep edge pressure gradient extend several neutral mean free paths inside the separatrix. In this section we try to identify 'cause and effect' physical relationships by which neutrals affect the pedestal structure.

We have already discussed the effect of the ionization of the influx of recycling and fueling neutrals in causing a peaking in the ion radial velocity profile just inside the separatrix, which in turn produced an increase in the negative ion pressure gradient just inside of the separatrix, as illustrated in Figs. 6. However, the edge peaking of the pinch velocity produced a larger effect on the edge pressure gradient in the shots considered in this paper. Thus, it is interesting to investigate whether the ionization of recycling and fueling neutrals also indirectly affected the edge pressure gradient through effects on the phenomena that caused the edge peaking in the pinch velocity.

Because we are modeling shots which are primarily fueled by the influx of recycling and injected neutrals, we can't just turn the neutrals off in the calculation and see what happens—we would no longer get a solution even remotely close to the experimental conditions. So we had to resort to a different stratagem to infer the magnitude of neutral ionization effects on the phenomena that cause the edge peaking in the pinch velocity. When we included the recycling and fueling neutrals in the particle balance but ignored their effect in the solution of the particle continuity equation (i.e. used a spatially constant Γ), we of course obtained a reduced edge peaking in the radial ion velocity $V_{ri} = \Gamma / n_i$ due only to the decreasing n_i. We also obtained a resulting factor of 2 reduction in the edge peaking in the pinch velocity due to using a constant Γ over the calculation region. The two effects combined to predict a reduction in the edge pressure gradient by a smaller factor, which when integrated inward from the separatrix predicted a pedestal with a larger width and about 70% of the original pedestal flattop density.

Thus, the direct mechanism by which the neutral influx contributes to the pedestal formation is to cause a peaking in the ion flux just inside the separatrix due to ionization. This peaking in the particle flux causes a peaking in the ion radial velocity $V_{ri} = \Gamma / n_i$ just inside the separatrix, which contributes directly to a strong negative pressure gradient $-(1/p_i)(dp_i/dr) = (V_{ri} - V_{pinch,i})/D_i$ just inside the separatrix. There are further indirect effects of the neutral ionization on the density profile--the effect of the peak in Γ on the particle and temperature distributions and the effect of the peaking in V_{ri} on V_θ, and hence on $V_{pinch,i}$. However, these indirect effects of neutral ionization do not dominate $V_{pinch,i}$, hence do not dominate the determination of the strong pressure gradient just inside the separatrix that causes the density pedestal structure, at least not in the shots that we have examined.

K. Diffusion coefficient

The diffusion coefficient of Eq. (3) is plotted for shots #9797 and #98893 in Fig. 9. The variation is caused mainly by the variations in collision frequency and momentum transfer frequency given in Figs. 1 and 5. The calculated diffusion coefficient clearly does not reduce significantly in the "steep-gradient" region relative to the "flattop" region for these shots.

III. ROTATION VELOCITIES AND RADIAL ELECTRIC FIELD

We established in the previous section that, given the experimental rotation and radial electric field profiles in the edge plasma and the experimentally inferred transport coefficients, the physical conservation requirements (particle, momentum, energy), the heat conduction transport relation, and atomic physics effects of recycling and fueling neutrals were sufficient to determine the observed density and temperature pedestal structure. We now turn the situation around and investigate if, given the profiles of heat and particle fluxes, plasma and neutral densities, and ion and electron temperatures determined in the previous section (and the experimentally inferred transport coefficients), the physical conservation, transport and atomic physics requirements are sufficient to determine the observed rotation and radial electric field profiles. In other words, we check to see if the calculation model of this paper contains an adequate representation of the particle, torque, and energy sources and the momentum transport mechanisms to enable calculation of the measured rotation velocities and radial electric field profiles from

the measured density and temperature profiles using the physical conservation, transport and atomic physics constraints.

A. Poloidal rotation

Equations for the poloidal rotation velocities were derived from poloidal momentum balance using a neoclassical expression for the parallel viscosity (Appendix C). These equations were solved numerically, using fixed density and temperature profiles calculated in the previous section and using $V_{\phi i}^0 = V_{\phi I}^0 = V_{\phi carbon}^{\exp}$ consistent with the assumptions of the previous section. (The subsequent calculation of toroidal rotation velocities for deuterium and carbon supports this approximation.) The results are shown in Figs. 10. The positive sense of the velocities is in the positive θ-direction in a right-hand (r-θ-φ) system with the positive φ-direction in the direction of the plasma current (fingers of the right hand in the positive θ-direction when right thumb in the plasma current direction). For these Co-injected shots, the positive sense of the poloidal rotation shown in Figs. 9 was downward at the outboard mid-plane.

Both the measured and calculated C VI poloidal rotation velocities are small, and there is no significant disagreement within the uncertainty of the measurements, except in the outer region in shot #118583, over roughly the same radial interval in which the measured and calculated toroidal rotation velocities are negative. The predicted deuterium poloidal rotation velocity is the same as the carbon rotation velocity for the highest pedestal density shot #98893, but departs progressively from the calculated carbon rotation velocity with decreasing collisionality, and the two calculated velocities had opposite signs for the least collisional shot #118583. With the possible exception of this outer region in shot #118583, the agreement of calculated and measured poloidal rotation velocities for carbon would seem to indicate that the relevant poloidal torques and momentum loss rates (neoclassical parallel viscosity, atomic physics) are being included in the poloidal rotation equations of appendix C.

B. Toroidal rotation

The toroidal momentum balance Eqs. (6) for ions and impurities can be summed to obtain an expression for the deuterium ion toroidal velocity

$$V_{\phi i}^0 = \frac{eZ_i B_\theta^0 \Gamma_i + \left(M_{\phi i} + M_{\phi I}\right) + e\left(n_i^0 Z_i + n_I^0 Z_I\right) E_\phi^A}{n_i^0 m_i \nu_{iI} \left(\beta_i + \beta_I\right)} + \frac{\beta_I \left(V_{\phi i}^0 - V_{\phi I}^0\right)}{\left(\beta_i + \beta_I\right)} \tag{16}$$

and then the impurity momentum balance equation can be solved for

$$V_{\phi I}^0 = \frac{V_{\phi i}^0}{\left(1+\beta_I\right)} + \frac{M_{\phi I} + n_I^0 eZ_I E_\phi^A}{n_i^0 m_i \nu_{iI} \left(1+\beta_I\right)} \tag{17}$$

The difference in species' toroidal rotation in Eq. (16) can be evaluated by subtracting the radial momentum balance equations for the two species to obtain Eq. (15) and using the difference in poloidal velocities calculated in the previous section, along with the difference in pressure gradients, to evaluate that expression.

The results of this calculation are compared with experiment in Figs. 11. Since Eq. (12) was used to solve the summed Eqs. (6) for ν_{di}^*, under the assumption $V_{\theta i}^0 = V_{\theta I}^0 = V_{\theta carbon}^{\exp}$, and then ν_{di}^* was used in the same set of equations, but without this assumption, to calculate the toroidal rotation in Eqs. (16) and (17), the agreement for the carbon toroidal velocities shown in Figs. 11 is a check on the assumption $V_{\phi i}^0 = V_{\phi I}^0 = V_{\phi carbon}^{\exp}$ used to evaluate Eq. (12) for ν_{di}^* and on the consistency of the overall calculation procedure. We have already drawn conclusions about the need for an additional input negative torque or momentum loss rate to explain the inferred ν_{di}^*.

C. Radial electric field

The radial electric field was calculated by evaluating the radial momentum balance of Eq. (13) for the carbon species, using the calculated values of the carbon pressure gradient and rotation velocities. The results are compared with the "measured" radial electric field, also constructed using Eq. (13) but with the measured values of the CVI pressure gradient and rotation velocities, in Figs. 12. The agreement is good except just inside the separatrix in shot #98893, where a much stronger negative peaking is predicted than measured; this is a result of the stronger predicted than measured negative carbon pressure gradient (i.e. to the inadequacy of the assumption in the calculation that the carbon concentration was uniform). Particularly noteworthy is that the measured negative well structure in the radial electric field for shot #118583 was predicted. The pressure gradient and rotation velocity components of E_r are also shown for shot #118583.

IV. SUMMARY AND CONCLUSIONS

A detailed analysis of the edge pedestal structure (density, temperature, rotation velocities, and radial electric field profiles) in three DIII-D H-mode discharges was carried out using equations based on the physical conservation (particles, three components of momentum, energy) and transport (heat conduction) requirements and including the atomic physics processes involving recycling and fueling neutrals. The calculation model was employed, together with experimental data, to infer the thermal and momentum transport coefficients, to relate the various measured profiles in the plasma edge for the purpose of identifying any missing particle, torque or energy sources and thermal and momentum transport processes in the model, and to identify the cause-and-effect relations that determine the edge pedestal structure---the overarching objectives of this paper.

The heat conduction and momentum transport coefficients were inferred from measured temperature and toroidal velocity profiles, as part of the overall computation procedure, and compared with theoretical predictions. The inferred thermal transport coefficients were of comparable magnitude to those predicted by simple prescriptions based on neoclassical and ion-temperature-gradient theory (ions) and electron-temperature-gradient theory (electrons). Toroidal angular momentum transport rates inferred from experiment were not fully accounted for over the entire steep-gradient and flattop region of the edge by neoclassical gyroviscous and atomic physics momentum transfer mechanisms, indicating a need for additional "anomalous" momentum transport or torque input mechanisms to explain the edge toroidal and poloidal rotation velocities profiles, and hence the radial electric field profile—a significant new result of this paper.

Next, the experimental rotation velocities and radial electric field profiles, the experimentally inferred transport coefficients, and the calculated fueling and recycling neutral influx were used together with the equations derived from the physical conservation, transport and atomic physics constraints to calculate the density and temperature profiles, which were in reasonable agreement with measured values, including the prediction of the observed edge density pedestal structure. These calculations confirmed our previous conclusion[7-9] that the principal mechanism for the edge density pedestal formation was the momentum balance requirement for a large negative pressure gradient to balance the force associated with the edge peaking of an inward particle pinch velocity and (to a lesser extent) the force associated with the edge peaking of the radial ion particle velocity. A new result of this paper was the demonstration that the edge peaking of the inward pinch velocity was driven via momentum balance by the observed edge peaking of the radial electric field and of the rotation velocities. The edge peaking of the radial ion particle velocity was required by the particle balance in the presence of an ionization source of recycling neutrals and by a decreasing plasma density in the edge.

Then the calculation was turned around. A set of equations for the poloidal and toroidal rotation velocities and the radial electric field was derived from the physical conservation, transport and atomic physics requirements. The density and temperature profiles calculated in the first part (which were close to the measured profiles), the particle and heat flux profiles calculated in the first part, the toroidal angular momentum transport coefficients inferred from experiment, and the influx of recycling and fueling neutrals calculated in the first part were used as input to solve this second set of equations. The calculated poloidal and toroidal rotation velocities profiles for carbon and the radial electric field profile generally agreed with experimental values within the uncertainty in the measurements. The agreement of toroidal velocities only confirmed the consistency of the calculation, since the experimentally inferred angular momentum transport coefficients were used in the calculation, but the agreement of poloidal velocities

confirmed that the important poloidal torques and momentum loss rates (neoclassical parallel viscosity, atomic physics) were being included in the poloidal rotation equations—a significant new result of this paper.

It was possible to obtain reasonable agreement between the calculated and measured temperature profiles in both the "flattop" and "steep-gradient" regions of the edge plasma ($\rho > 0.85$) by using a radially constant value of the inferred thermal conduction coefficient in two of the three shots considered. Moreover, the calculated diffusion coefficient decreased only slightly in the steep-gradient region in one shot, while increasing in the other two. Thus, it seems that the steep-gradient-region in the edge of H-mode shots is not necessarily associated with a sharp decrease in transport coefficients, as is commonly thought—another new result of this paper. The inferred and calculated particle and heat transport coefficients in the edge were smaller than are usually inferred either in the core of H-mode plasmas or the edge of L-mode plasmas, consistent with other observations.

A secondary objective of this investigation was to better understand the physical mechanisms by means of which recycling and fueling neutrals affected the edge pedestal structure. Our calculations indicated that the observed density pedestals were caused by the momentum balance requirement for a steep negative pressure gradient to balance forces associated with edge peaking an inward pinch velocity and in an outward radial ion particle velocity. The ionization of recycling and fueling neutrals in the edge directly caused the peaking in the outward radial particle velocity, but this term was calculated to be less important than the inward pinch velocity, in the shots considered. The neutral influx also affects the terms that constitute the inward pinch velocity in at least two ways: 1) the edge peaking in the radial particle velocity produces a peaking in the $eV_r \times B_\phi$ torque in the poloidal momentum balance equations that contributes to the edge peaking in V_θ; and 2) charge exchange, elastic scattering and ionization constitute angular momentum damping mechanisms that affect the toroidal and poloidal rotation velocities in the edge; both of which in turn affect the radial electric field. Subsidiary calculations indicated that the first above indirect effect on the pinch velocity plus the direct effect of the edge peaking in the radial particle flux could account for ≈ 30% of the edge pressure gradient requirement being due to neutrals—another interesting new result. There may be other effects of the neutral influx that have not been taken into account in the calculations.

Further efforts along this line of investigation are suggested by the above discussion: 1) detailed gyro-kinetic or gyro-fluid thermal transport calculations in the plasma edge to obtain more accurate predictions of ion and electron thermal diffusivities; 2) investigation of torque input and angular momentum transport mechanisms in the plasma edge in addition to those included in the calculation model of this paper, including kinetic phenomena; 3) improvement of some of the approximations made in implementing the physical conservation and transport constraints (e.g. uniform impurity concentration); 4) improvement in solution procedures for the constraint equations; and 5) further detailed analysis of measured edge profiles.

Appendix A: Thermal Transport Coefficients

Neoclassical

The Chang-Hinton expression for the ion thermal conductivity is[23]

$$\chi_i^{ch} = \varepsilon^{1/2} \rho_{i\theta}^2 \nu_{ii} \left[a_1 g_1 + a_2 (g_1 - g_2) \right] \qquad \text{(A1)}$$

where the *a*'s account for impurity, collisional and finite inverse aspect ratio effects and the *g*'s account for the effect of the Shafranov shift. These parameters are collected in the appendix to Ref. 7.

In the presence of a strong shear in the radial electric field, the particle banana orbits are squeezed, resulting in a reduction in the ion thermal conductivity by a factor of $S^{-3/2}$, where[24]

$$S = \left| 1 - \rho_{i\theta} \left(\frac{d \ln E_r}{dr} \right) \left(\frac{E_r}{\upsilon_{thi} B_\theta} \right) \right| \qquad \text{(A2)}$$

Here $\rho_{i\theta}$ is the ion poloidal gyroradius.

Ion temperature gradient modes

For a sufficiently large ion temperature gradient $\left(L_{Ti} < L_{Ti}^{crit} \approx 0.1R\right)$ the toroidal ion temperature gradient (ITG) modes become unstable. An estimate of the ion thermal conductivity due to ITG modes is[25]

$$\chi_i^{itg} = \frac{5}{2}\left(\frac{1}{RL_{Ti}}\right)^{1/2}\left(\frac{T_e}{m_i}\right)\left(\frac{m_i}{e_i B}\right)\frac{1}{2}\rho_i \qquad \text{(A3)}$$

where ρ_i is the gyroradius in the magnetic field *B*, and $k_\perp \rho_i = 2$ has been used..

Electron temperature gradient modes

The electron temperature gradient (ETG) modes (electrostatic drift waves with $k_\perp c_s \le \omega_{pe}$) are unstable when $\eta_e \equiv L_n / L_{Te} \ge 1$. An expression for the thermal conductivity due to the ETG modes is given by[26]

$$\chi_e^{etg} = 0.13\left(\frac{c_s}{\omega_{pe}}\right)^2 \frac{\upsilon_{the} S_m}{qR}\eta_e\left(1+\eta_e\right) \qquad \text{(A4)}$$

where $S_m \equiv (r/q)(dq/dr)$ is the magnetic shear and ω_{pe} is the electron plasma frequency.

Appendix B: Neoclassical viscous and inertial momentum transport frequencies

Viscous "Drag"

The largest component of neoclassical viscosity that enters the flux surface averaged toroidal momentum balance equation is the gyroviscous component[27-30]. An expression for the neoclassical gyroviscous momentum transfer, or drag, frequency can be derived[28] in toroidal geometry by using the representations $R = R_0\left(1+\varepsilon\cos\theta\right)$ and $B = B^0/\left(1+\varepsilon\cos\theta\right)$, replacing the radial gradients by gradient scale lengths (e.g. $L_n^{-1} = -1/n\,\partial n/\partial r$), and expanding the poloidal dependence of densities and velocities in a low-order Fourier series of the form

$$n_j(r,\theta) = n_j^0\left[1 + n_j^c(r)\cos\theta + n_j^s(r)\sin\theta\right] \qquad \text{(B1)}$$

to obtain a representation of the toroidal viscous torque in terms of an angular momentum transfer, or "drag", frequency, ν_{dj}

$$\left\langle R^2\nabla\phi\cdot\nabla\cdot\boldsymbol{\pi}_j\right\rangle_{gv} \approx \frac{1}{2}\tilde{\theta}_j G_j \frac{n_j m_j T_j}{e_j B_\phi}\frac{V_{\phi j}^0}{\bar{R}} \equiv R n_j m_j \nu_{dj} V_{\phi j}^0 \qquad \text{(B2) where}$$

$$\begin{aligned}\tilde{\theta}_j &\equiv \left(4+\tilde{n}_j^c\right)V_{\phi j}^s + \tilde{n}_j^s\left(1-V_{\phi j}^c\right)\\ &= \left(4+\tilde{n}_j^c\right)\left(-\left(V_{\theta j}/V_{\phi j}\right)\left(\Phi^s+\tilde{n}_j^s\right)+\Phi^s\left(1+\left(P_j'/V_{\phi j}\right)\right)\right)+\\ &\quad \tilde{n}_j^s\left(\left(V_{\theta j}/V_{\phi j}\right)\left(\Phi^c+\tilde{n}_j^c+2\right)-\Phi^c\left(1+\left(P_j'/V_{\phi j}\right)\right)\right)\end{aligned} \qquad \text{(B3)}$$

represents poloidal asymmetries and

$$G_j \equiv -\frac{r}{\eta_{4j} V_{\phi j}} \frac{\partial \left(\eta_{4j} V_{\phi j} \right)}{\partial r} = r \left(L_n^{-1} + L_T^{-1} + L_{V_\phi}^{-1} \right) \tag{B4}$$

represent radial gradients. We have used the gyroviscosity coefficient $\eta_{4j} \approx n_j m_j T_j / e_j B$ and introduced the notation

$$\hat{V}_{\theta j} \equiv \frac{V_{\theta j}^0}{f \upsilon_{thj}}, \hat{V}_{\phi j} \equiv \frac{V_{\phi j}^0}{\upsilon_{thj}}, \hat{P}_j' \equiv \frac{1}{n_j^0 e_j B_\theta^0 \upsilon_{thj}} \frac{\partial \overline{p_j}}{\partial r}, \; f_p \equiv \frac{B_\theta}{B_\phi}, \tilde{n}_j^{c/s} \equiv \frac{n_j^{c/s}}{\varepsilon}, \hat{\Phi}^{c/s} \equiv \frac{\Phi^{c/s}}{\varepsilon} = \frac{n_e^{c/s}}{\varepsilon \left(e\Phi / T_e \right)} \tag{B5}$$

with the last relation following from electron momentum balance, and neglected radial gradients in the density asymmetry coefficients $n_j^{c,s}$.

The radial gradient scale lengths needed to evaluate the G_j from Eq. (B4) are taken from experiment, and the density asymmetries needed to evaluate $\hat{\theta}_j$ from Eq. (B3) from the poloidal momentum equations described in appendix C.

Inertial "drag"

The toroidal component of the inertial term in the angular momentum balance equation in toroidal geometry is

$$R^2 \nabla \phi \cdot n_j m_j \left(\mathbf{V}_j \cdot \nabla \right) \mathbf{V}_j = R n_j m_j \left(V_{rj} \frac{\partial V_{\phi j}}{\partial r} + \frac{V_{rj} V_{\phi j}}{R} - \frac{V_{\phi j}}{r} \frac{\partial V_{\theta j}}{\partial \theta} - \frac{V_{\phi j} V_{\theta j}}{R} \sin\theta \right) \tag{B6}$$

Flux surface averaging and following a procedure similar to that outlined above leads to an equivalent expression for the "inertial drag" term

$$\nu_{nj} \equiv V_{rj} \left[\frac{1}{R_0} - \frac{1}{L_{v\phi}} \right] - \frac{1}{2} \frac{\varepsilon V_{\theta j}^0}{R_0} \left[-\hat{V}_{\theta j}^c \left(\hat{V}_{\phi j}^s + \tilde{n}_j^s \right) + V_{\theta j}^s \left(\left(2 + \hat{V}_{\phi j}^c + \tilde{n}_j^c \right) + \left(\hat{V}_{\theta j}^s + \hat{V}_{\phi j}^s + \tilde{n}_j^s \right) \right) \right] \tag{B7}$$

where

$$\hat{V}_{\theta j}^s = \tilde{I}_j^s B_\theta^0 \Big/ \varepsilon n_j^0 - \tilde{n}_j^s V_{\theta j}^0, V_{\theta j}^c = \tilde{I}_j^c B_\theta^0 \Big/ \varepsilon n_j^0 - \left(1 + \tilde{n}_j^c \right) V_{\theta j}^0 \tag{B8}$$

and the quantities

$$\tilde{I}_j^s = r \hat{S}_j^c, \tilde{I}_j^c = -r \hat{S}_j^s \tag{B9}$$

represent the sine and cosine components of the asymmetry in the ionization source.

Appendix C: Poloidal rotation and density asymmetry calculation

We follow and extend somewhat our previous work[31] to develop equations for the poloidal rotation velocities and density asymmetries in the plasma edge in this section. The poloidal component of the momentum balance equation for ion species "j" is

$$\begin{aligned} & n_j m_j \left[\left(\mathbf{V}_j \cdot \nabla \right) \mathbf{V}_j \right]_\theta + \left[\nabla \cdot \Pi_j \right]_\theta + \frac{1}{r} \frac{\partial p_j}{\partial \theta} - M_{\theta j} - F_{\theta j} + \\ & n_j e_j \left(V_{rj} B_\phi - E_\theta \right) + m_j \left(n_j \nu_{elcx} + V_{\theta j} \right) \hat{S}_j = 0 \end{aligned} \tag{C1}$$

where $S_j - \left\langle S_j \right\rangle \equiv \tilde{S}_j$ and the poloidal components of the inertial and viscous terms are

$$n_j m_j \left[\left(\mathbf{V}_j \cdot \nabla \right) \mathbf{V}_j \right]_\theta = n_j m_j \left[V_{rj} \frac{\partial V_{\theta j}}{\partial r} + \frac{V_{rj} V_\theta}{r} + \frac{1}{2} \frac{1}{r} \frac{\partial V_{\theta j}^2}{\partial \theta} + \frac{V_{\phi j}^2}{R} \sin\theta \right] \tag{C2}$$

and

$$\left[\nabla \cdot \Pi_j \right]_\theta = \eta_{0j} \left(\frac{1}{2} A_{oj} \right) \left\{ \frac{1}{r} \frac{\partial \ln\left(\eta_{0j} A_{oj} \right)}{\partial \theta} - 3 \frac{\sin\theta}{R} \right\} \tag{C3}$$

where

$$A_0 = 2 \left\{ -\frac{1}{3} \left(\frac{\partial V_p}{\partial l_p} \right) + \left[\left(\frac{1}{R} \right) \frac{\partial R}{\partial l_p} + \frac{1}{3} \left(\frac{1}{B_p} \right) \frac{\partial B_p}{\partial l_p} \right] V_p + f_p R \frac{\partial \left(V_\phi / R \right)}{\partial l_p} \right\} \tag{C4}$$

and the neoclassical parallel viscosity coefficient is represented by[32]

$$\eta_{0j} = \frac{n_j m_j \upsilon_{thj} q R \varepsilon^{-3/2} \nu_{jj}^*}{\left(1 + \varepsilon^{-3/2} \nu_{jj}^* \right) \left(1 + \nu_{jj}^* \right)} \equiv n_j m_j \upsilon_{thj} q R f_j \left(\nu_{jj}^* \right) \tag{C5}$$

where $\nu_{jj}^* = \nu_{jj} q R / \upsilon_{thj}$ and $\varepsilon = r/R$.

Making low-order Fourier expansions of the form

$$n_j \left(r, \theta \right) = n_j^0 \left(r \right) + n_j^s \sin\theta + n_j^c \cos\theta \tag{C6}$$

and taking the flux surface average with weighting functions 1, $\sin\theta$ and $\cos\theta$ results in a coupled set of equations (three times the number of ion species) that can be solved for the $V_{\theta j}^0$ and $\tilde{n}_j^{s,c}$ for all the plasma ion species. If the first term on the right in Eq. (C2) is neglected, these equations can be solved locally on each radial flux surface. The justification for this neglect would be the plausible assumption $V_{rj} << V_{\theta j} < V_{\phi j}$, which would also justify neglect of the second term on the right in Eq. (C2), relative to the last two terms. The resulting equations are

$$\begin{aligned}
&\bar{V}_{\theta j} \left[-q \bar{V}_{\phi j} \varepsilon \left(\tilde{n}_j^s + \bar{\Phi}^s \right) - q^2 f_j f_p \left(1 + \bar{\Phi}^c + \frac{2}{3} \tilde{n}_j^c \right) + f_p \sum_{k \neq j} \nu_{jk}^* + \right. \\
&\frac{q}{\varepsilon} \nu_{elcx,j}^* f_p + \frac{1}{2} f_p \varepsilon \nu_{ionj}^* \left\{ \left(1 + \tilde{n}_j^c \right) \left(\frac{n_e^0}{n_j^0} \left(\tilde{n}_e^c + \tilde{n}_{oj}^c \right) - \left(\tilde{n}_j^c + \tilde{n}_{oj}^c \right) \right) + \right. \\
&\left. \left. \tilde{n}_j^s \left(\frac{\bar{n}_e}{n_j} \left(\tilde{n}_e^s + \tilde{n}_{oj}^s \right) - \left(\tilde{n}_j^s + \tilde{n}_{oj}^s \right) \right) \right\} \right] - \sum_{k \neq j} \bar{V}_{k\theta} \left[f_p \nu_{jk}^* \sqrt{\frac{m_j}{m_k}} \right] = \\
&-\bar{V}_{rj} - q\varepsilon \frac{1}{4} \tilde{n}_j^s - q\varepsilon \bar{\Phi}_j \left[\frac{1}{4} \left(\bar{\Phi}^s + \tilde{n}_j^c \bar{\Phi}^s - \tilde{n}_j^s \bar{\Phi}^c \right) \right] - q^2 f_j f_p \left(\bar{V}_{\phi j} + \bar{P}_j' \right) \bar{\Phi}^c \\
&-q\varepsilon \bar{V}_{\phi j} \left[\left(\bar{V}_{\phi j} + \bar{P}_j' \right) \bar{\Phi}^s + \frac{1}{2} \bar{V}_{\phi j} \tilde{n}_j^s \right] - \frac{n_e^0}{n_j^0} \nu_{ionj}^* q \left[\bar{V}_{\phi j} \varepsilon \left(\tilde{n}_e^c + \tilde{n}_{oj}^c \right) \right. \\
&\left. -\frac{2}{3} q f_j \left(\tilde{n}_e^s + \tilde{n}_{oj}^s \right) \right]
\end{aligned} \tag{C7}$$

$$
\begin{aligned}
&\tilde{n}_j^s\left[\frac{1}{3}\frac{q^2}{\varepsilon}f_j f_p \hat{V}_{\theta j}+\frac{1}{2}\varepsilon\hat{V}_{rj}-\frac{1}{2}\varepsilon f_p\sum_{k\neq j}\nu_{jk}^*\hat{V}_{\theta k}\sqrt{\frac{m_j}{m_k}}+\frac{1}{2}q\nu_{ion}^* f_p\hat{V}_{\theta j}\right]\\
&+\tilde{n}_j^c\left[\frac{1}{2}qf_p^2\hat{V}_{\theta j}^2-\frac{1}{4}q+\frac{1}{2}q\nu_{elcx,j}^*\nu_{ionj}^*\right]=-\frac{1}{2}\varepsilon f_p\sum_{k\neq j}\nu_{jk}^*\hat{V}_{\theta j}\tilde{n}_k^s\\
&-\frac{1}{4}q\hat{\Phi}_j\left[-\overline{\Phi}^c\right]-\frac{q^2}{\varepsilon}f_j f_p\left[\frac{1}{2}\left(\hat{V}_{\theta j}-\hat{V}_{\phi j}-\hat{P}'_j\right)\Phi^s-\frac{1}{2}qf_p^2\hat{V}_{\theta j}^2-\frac{1}{2}q\hat{V}_{\phi j}^2\right.\\
&-\frac{1}{2}q\nu_{elcx,j}^*\left[f_p\hat{V}_{\theta j}\tilde{n}_{oj}^s+\nu_{ionj}^*\tilde{n}_{oj}^c\right]-q\nu_{ionj}^* f_p\left[\frac{1}{2}\hat{V}_{\theta j}\left\{\tilde{n}_{oj}^s\left(1+\frac{n_e^0}{n_j^0}\right)+\frac{n_e^0}{n_j^0}\tilde{n}_e^s\right\}\right.\\
&\left.\left.+\frac{1}{3}\frac{q}{\varepsilon}f_j\frac{n_e^0}{n_j^0}\left(\tilde{n}_e^c+\tilde{n}_{oj}^c\right)\right]\right]
\end{aligned}
\tag{C8}
$$

and

$$
\begin{aligned}
&\tilde{n}_j^c\left[\frac{1}{3}\frac{q^2}{\varepsilon}f_j f_p \hat{V}_{\theta j}+\frac{1}{2}\varepsilon\hat{V}_{rj}-\frac{1}{2}\varepsilon f_p\sum_{k\neq j}\nu_{jk}^*\hat{V}_{\theta k}\sqrt{\frac{m_j}{m_k}}+\frac{1}{2}q\nu_{ionj}^* f_p\hat{V}_{\theta j}\right]\\
&+\tilde{n}_j^s\left[-\frac{1}{2}qf_p\hat{V}_{\theta j}^2+\frac{1}{4}q-\frac{1}{2}q\nu_{elcx,j}^*\nu_{ionj}^*\right]=-\sum_{k\neq j}\tilde{n}_k^c\left[\frac{1}{2}\varepsilon f_p\nu_{jk}^*\hat{V}_{\theta j}\right]\\
&-\frac{1}{4}q\hat{\Phi}_j\left[\Phi^s\right]-\frac{q^2}{\varepsilon}f_j f_p\left[\frac{1}{2}\left\{\left(1+\Phi^c\right)\hat{V}_{\theta j}-\left(\hat{V}_{\phi j}-\hat{P}_j'\right)\Phi^c\right\}\right]\\
&-q\hat{V}_{\phi j}^2\left[\frac{1}{4}\varepsilon\left\{\hat{V}_{\phi j}^s\hat{V}_{\phi j}^c+\tilde{n}_j^c\hat{V}_{\phi j}^s+\tilde{n}_j^s\hat{V}_{\phi j}^c\right\}\right]-\frac{1}{2}q\nu_{elcx,j}^*\left[f_p\hat{V}_{\theta j}\tilde{n}_{oj}^c-\nu_{ionj}^*\tilde{n}_{oj}^s\right]\\
&-qf_p\nu_{ionj}^*\left[\frac{1}{2}\hat{V}_{\theta j}\left\{\tilde{n}_{oj}^c\left(1+\frac{n_e^0}{n_j^0}\right)+\frac{n_e^0}{n_j^0}\tilde{n}_e^c\right\}+\frac{1}{3}\frac{q}{\varepsilon}f_j\frac{n_e^0}{n_j^0}\left(\tilde{n}_e^s+\tilde{n}_{oj}^s\right)\right]
\end{aligned}
\tag{C9}
$$

where

$$
\hat{V}_{rj}\equiv\frac{V_{rj}^0}{\left(\frac{m_j\upsilon_{thj}}{e_j B_\phi^0}\right)\left(\frac{\upsilon_{thj}}{qR}\right)},\quad \hat{\Phi}_j\equiv\frac{e_j\Phi^0}{T_j},
$$

$$
\nu_{jk}^*\equiv\frac{\nu_{jk}^0}{\frac{\upsilon_{thj}}{qR}},\quad \nu_{ionj}^*\equiv\frac{\left(\nu_{ionj}^0+\nu_{ionj,nb}^0\right)r}{\upsilon_{thj}},\quad \nu_{elcx,j}^*\equiv\frac{\nu_{elcx,j}^0 r}{\upsilon_{thj}},
\tag{C10}
$$

In the above, ν_{ionj}^0 is the ionization frequency of recycling and gas fueling neutrals, $\nu_{ionj,nb}^0=S_{nbj}^0/n_j^0$ is the ionization frequency of neutral beam particles, and $\nu_{elcx,j}^0$ is the charge-exchange plus elastic scattering frequency of 'cold' recycling neutrals.

REFERENCES

1. A. E. Hubbard, Plasma Phys. Control. Fusion, 42, A283 (2000).
2. M. Kotschenreuther, W. Dorland, Q. P. Liu, *et al*., Proc.16th Conf. Plasma Phys Control. Fusion Res., Montreal, 1996 (IEAE, Vienna, 1997), Vol. 2, p 371.
3. J. E. Kinsey, R. E. Waltz and D. P. Schissel, Proc. 24th Eur. Phys. Soc., Berchtesgarten, 1997, Vol. III, p 1081.
4. J. W. Connor, R. J. Hastie, H. R. Wilson and R. L. Miller, Phys. Plasmas, 5, 2687 (1998).
5. P. B. Snyder, H. R. Wilson, J. R. Ferron, *et al*., Phys. Plasmas, 9, 2037, (2002).
6. P. B. Snyder, H. R. Wilson, J. R. Ferron, *et al*., Nucl. Fusion, 44, 320 (2004).
7. W. M. Stacey, Phys. Plasmas, 11, 1511 (2004).
8. W. M. Stacey, Phys. Plasmas, 11, 5487 (2004).
9. W. M. Stacey and R. J. Groebner, Phys. Plasmas, 12, 042504 (2005).
10. C. S. Chang, S. Ku and H. Weitzner, Phys. Plasmas, 11, 2649 (2004).
11. R. J. Groebner, M. A. Mahdavi, A. W. Leonard, *et al*., Phys. Plasmas, 9, 2134 (2002).
12. R. J. Groebner, M. A. Mahdavi, A. W. Leonard, *et al*., Nucl. Fusion, 44, 204 (2004).
13. W. M. Stacey and R. J. Groebner, Phys. Plasmas, 10, 2412 (2003).
14. R. J. Groebner and T. H. Osborne, Phys. Plasmas, 5, 1800 (1998).
15. T. Onjun, G. Bateman, A. Kritz, *et al*., Phys. Plasmas, 9, 5018 (2002).
16. W. Suttrop, O. Gruber, B. Kurzan, *et al*., Plasma Phys. Control. Fusion, 42, A97 (2000).
17. T. H. Osborne, J. R. Ferron, R. J. Groebner, *et al*., Plasma Phys. Control Fusion, 42, A175 (2000).
18. W. M. Stacey, Phys. Plasmas 5, 1015 (1998); 8, 3673 (2001).
19. W. M. Stacey, Nucl. Fusion, 40, 965 (2000).
20. L. D. Horton, A. V. Chankin, Y. P. Chen, *et al.*, Nucl. Fusion, 45, 856 (2005).
21. L. R. Baylor, K. H. Burrell, R. J. Groebner, *et al*., Phys. Plasmas, 11, 3100 (2004).
22. H. A. Claassen, H. Gerhauser, A. Rogister, *et al.,* Phys. Plasmas, 7, 3699 (2000).
23. C. S. Chang and F. L. Hinton, Phys. Fluids, 29, 3314 (1986).
24. K. C. Shaing and R. D. Hazeltine, Phys. Fluids B, 4, 2547 (1992).
25. F. Romanelli, W. M. Tang and R. B. White, Nucl. Fusion, 26, 1515 (1986).
26. J. A. Wesson, *Tokamaks,* 2nd ed. (Clarendon Press, Oxford, 1997).
27. S. I. Braginskii, Rev. Plasma Phys., 1, 205 (1965).
28. A. B. Mikhailovskii and V. S. Tsypin, Sov. J. Plasma Phys., 10, 51 (1984).
29. W. M. Stacey and D. J. Sigmar, Phys. Fluids, 28, 2800 (1985).
30. P. J. Catto and A. N. Simakov, Phys. Plasmas, 12, 012501 (2005).
31. W. M. Stacey, Phys. Plasmas, 9, 3874 (2002).
32. W. M. Stacey, A. W. Bailey, D. J. Sigmar and K. C. Shaing, Nucl. Fusion, 25, 463 (1985).

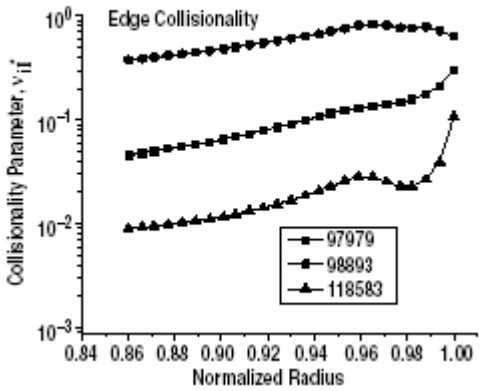

Fig. 1 Normalized deuterium-carbon collisionality parameter $\nu_{il}^* = \nu_{il} qR/\upsilon_{thi}$.

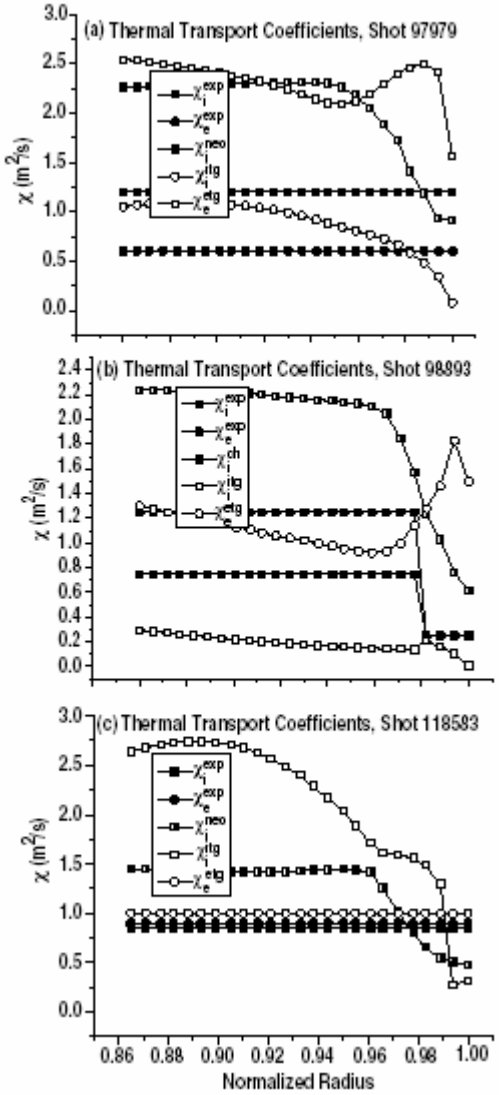

Fig. 2 Thermal transport coefficients inferred from experiment (solid symbols) compared with theoretical estimates from neoclassical, ITG and ETG theories.

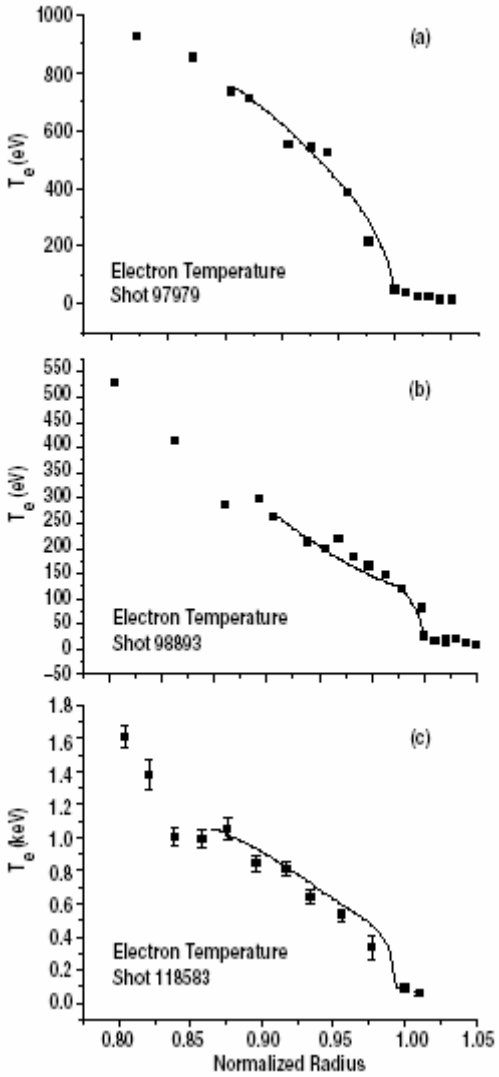

Fig. 3 Calculated (solid line) and measured electron temperatures.

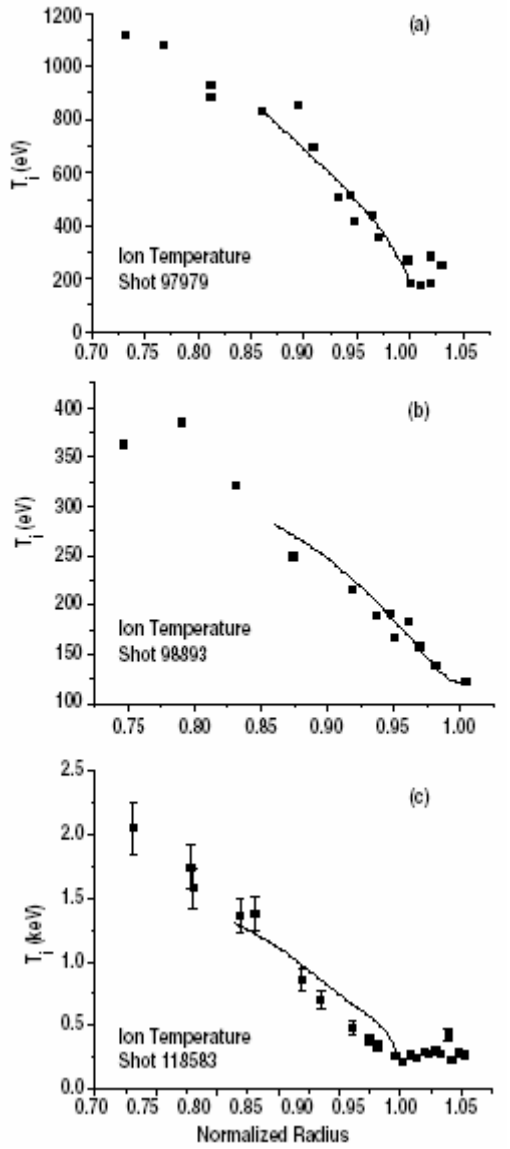

Fig. 4 Calculated (solid line) and measured ion temperatures.

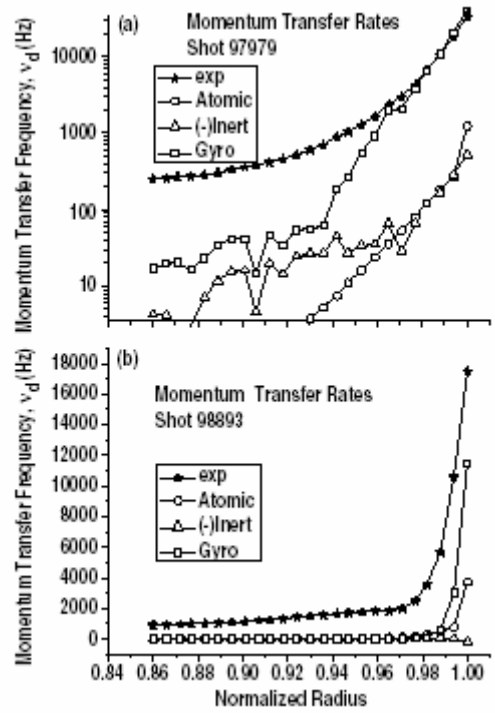

Fig. 5 Total frequency for the radial transfer of toroidal angular momentum inferred from experiment (solid stars) compared with calculated angular momentum transfer frequencies due to atomic physics, inertial effects and neoclassical gyroviscosity.

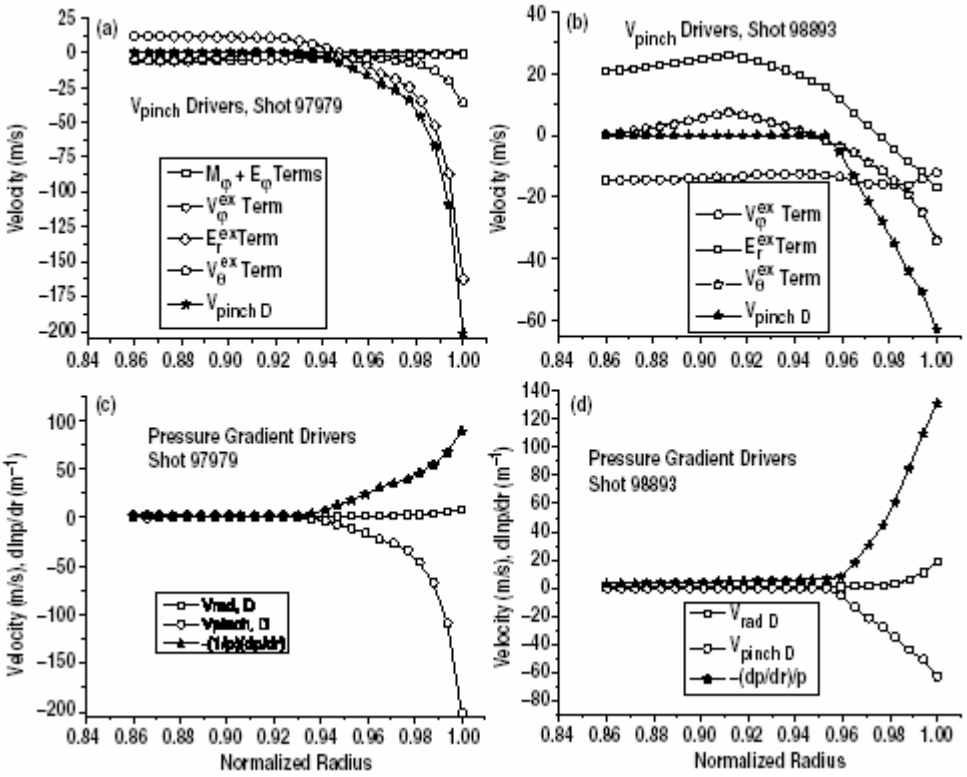

Fig. 6 Phenomenological causes of the edge pressure pedestal: a) and b) phenomena contributing to the inward deuterium pinch velocity; and c) and d) contributions of the inward pinch velocity and the radial particle velocity to the deuterium pressure gradient.

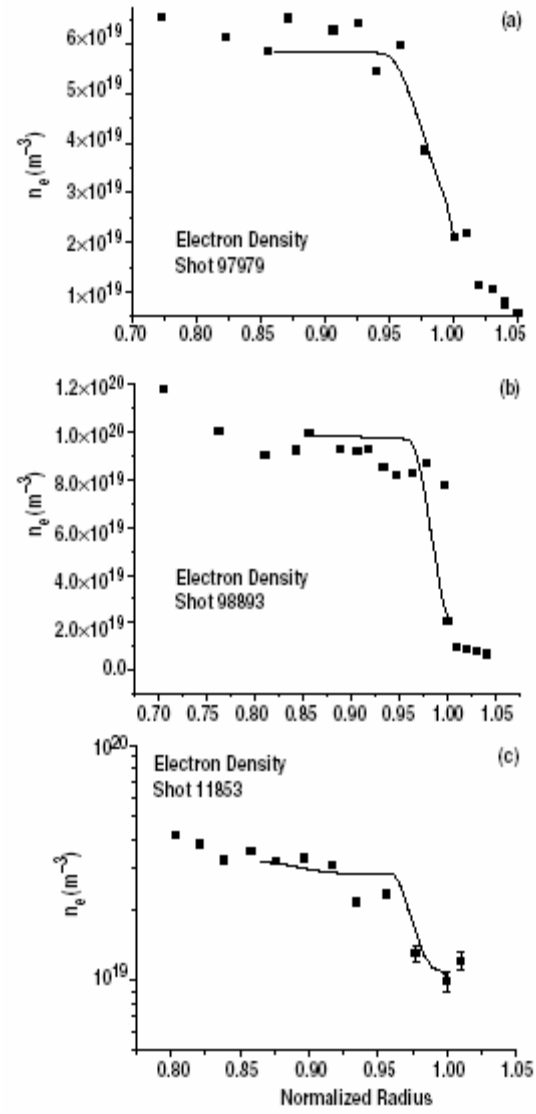

Fig. 7 Calculated (solid line) and measured electron densities.

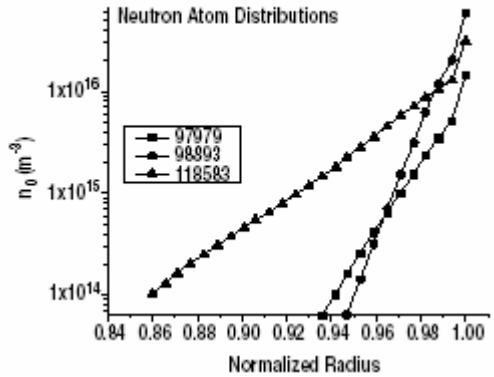

Fig. 8 Calculated neutral densities.

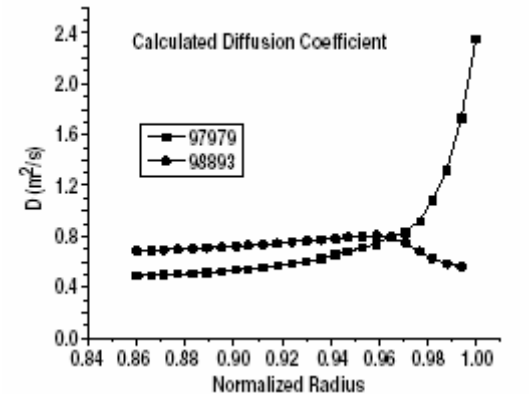

Fig. 9 Calculated diffusion coefficients.

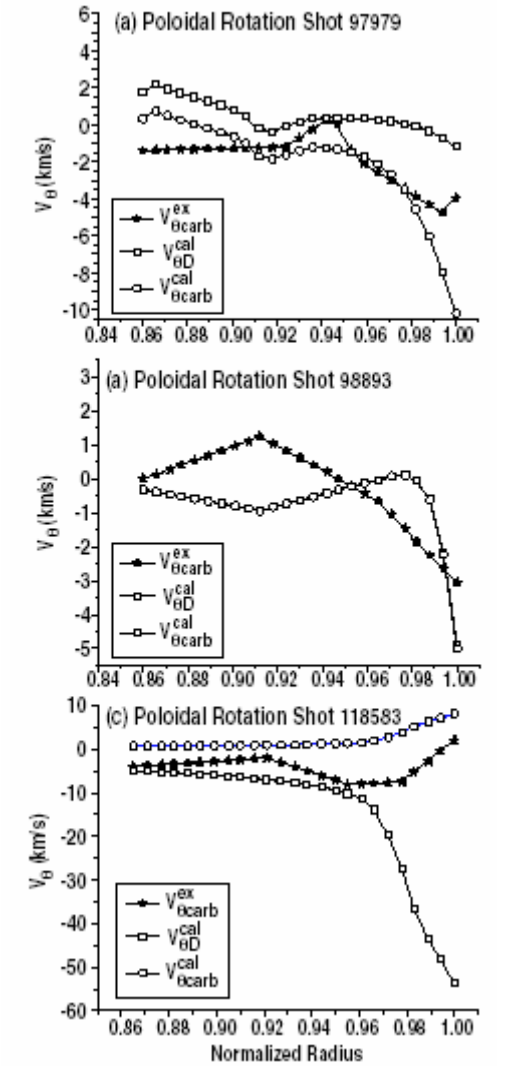

Fig. 10. Calculated deuterium and carbon poloidal rotation velocities (empty symbols) from poloidal momentum balance using neoclassical parallel viscosity compared with measured carbon VI poloidal rotation velocity (solid star). Note that the sign convention is different for the calculated and measured velocities.

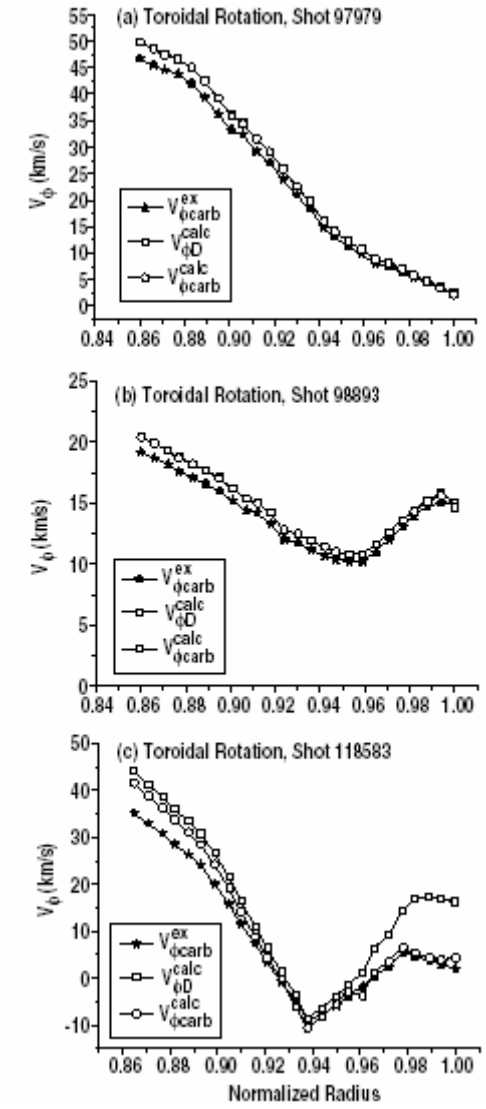

Fig. 11 Calculated deuterium and carbon toroidal rotation velocities (empty symbols) from toroidal momentum balance using same inferred momentum transfer frequency compared with measured carbon VI toroidal rotation velocity (solid star).

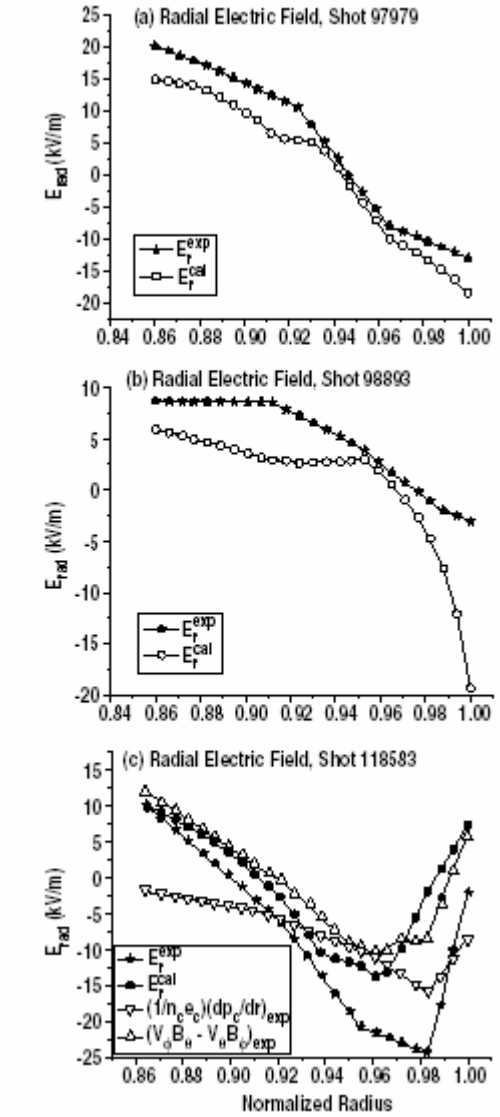

Fig. 12 Calculated radial electric field from radial momentum balance for carbon using calculated carbon pressure gradient and rotation velocities (circle symbol) compared with the experimental radial electric field calculated the same way but using measured carbon VI pressure gradient and rotation velocities (solid star). Also shown are the pressure gradient and VxB components of the experimental radial electric field.